Article

Crack Initiation in Ni-Based Single Crystal Superalloy under Low-Cycle Fatigue-Oxidation Conditions

Pengfei Wang [1], Xinbao Zhao [1,2,*], Quanzhao Yue [1], Wanshun Xia [1,*], Qingqing Ding [1], Hongbin Bei [1], Yuefeng Gu [1,2,*] and Ze Zhang [1,2]

1   Institute of Superalloys Science and Technology, School of Materials Science and Engineering, Zhejiang University, Hangzhou 310027, China
2   State Key Laboratory of Silicon Materials, School of Materials Science and Engineering, Zhejiang University, Hangzhou 310027, China
*   Correspondence: superalloys@zju.edu.cn (X.Z.); wanshunxia@zju.edu.cn (W.X.); guyf@zju.edu.cn (Y.G.)

Abstract: The mechanism of oxidation-assisted initiation of surface cracks of a fourth-generation Ni-based single crystal superalloy was systematically investigated during low cycle fatigue at 900 °C and 980 °C. The results show that cracks initiate near the surface defects at 900 °C, while they initiate in the surface oxide layer at 980 °C. At 900 °C, the oxidation microcrack initiation in the thicker inner oxidation layer is difficult to connect with the surface oxidation crack, which is an essential reason for the crack growth rate being slower and not becoming the main crack. At 980 °C, microcracks form in the outer oxide layer and quickly connect with microcracks at the surface and inner/outer oxide layer interface, growing into long cracks that become channels for rapid oxygen transport. This accelerates the crack growth rate, and eventually the oxide crack becomes the main crack.

Keywords: oxidation; low-cycle fatigue; crack initiation; single crystal superalloy

1. Introduction

Nickel-based single crystal superalloy has excellent corrosion resistance and high temperature mechanical properties; it is a key material for aeroengine turbine blades [1,2]. The oxidation reaction of nickel-based single crystal superalloys inevitably occurs when they are serviced at elevated temperatures. Although the surface of superalloy is normally covered with a layer of anti-corrosion and anti-oxidation thermal barrier coating during service, the coating and the alloy matrix do not belong to the same whole, and the thermal expansion coefficient between the thermal barrier coating and the alloy is different. In addition, damage due to foreign objects or other causes may occur. These factors may result in local spalling and failure of the thermal barrier coating [3–5]. In the area where the thermal barrier coating is peeled off, the alloy becomes directly exposed to the elevated-temperature oxidation environment, the alloy oxidizes, and the oxidized area may become the source of defects and cracks that considerably reduce the mechanical properties [6].

In addition to elevated temperature, turbine blades are subjected to complex stress changes during operation that result in fatigue, creep, and other failure forms [1,5,7,8]. Low cycle fatigue is one of the critical causes of turbine blade failure. Low-cycle fatigue, otherwise known as strain fatigue, refers to fatigue with elevated cyclic stress level. Plastic strain and low cycle times (cycle times below 10^5) play a leading role. The locations of low-cycle fatigue failure in turbine blades are mainly in areas where stress is concentrated, such as the lower part of the blade body, blade roots, pores, and corners [1,7,9]. With the improvement of aero-engine efficiency requirements, the use temperature of the alloy continues to increase [10]. In addition to the atomic diffusion rate and the temperature of stress concentration, the alloy faces more serious stress and oxidation problems. Therefore, low-cycle fatigue behavior under high temperature oxidation environments has become the focus of research on nickel-based single crystal superalloys [1,11,12].

The effect of temperature on crack initiation is mainly related to high-temperature oxidation. The formation of cracks in surface oxides that can split into different oxide layers is mainly due to the different thermal expansion coefficients between the oxide layer and the alloy matrix, which is prone to stress concentration and crack formation [13–15]. The higher the temperature, the faster the oxidation rate, the easier the crack initiation at the oxide layer [16,17]. Most of the current research on the mechanism of crack initiation in oxide layers has focused on thermal exposure experiments. After the initiation of the crack from the surface oxide layer, it barely grows into the matrix, while the rapid growth of the oxide crack into the matrix leads to fatigue fracture. Due to the high stress and rapid crack propagation in low-cycle fatigue, cracks can grow inward relatively quickly. As the stage from crack initiation to main crack development accounts for the majority of the lifetime, this stage is an essential component of low-cycle fatigue studies. Research [18–22] shows that with the increase of temperature, the crack initiation location gradually changes from internal defects to external defects. The internal defects are mostly micropores and the external defects are mostly oxidation defects. There is a well-defined transition temperature as a function of crack initiation location, crack growth rate, and defect type shift. However, there has been little discussion on how cracks are initiated and grow in different oxidation layers.

Therefore, this study mainly focuses on the initiation and growth of microcracks in different oxidation layers during low-cycle fatigue, as well as the effect of temperature on this process, in order to better understand the effect of high-temperature oxidation on the initiation pattern of the main crack.

2. Material and Experimental Procedure

The material used in this study was a test bar of a fourth-generation nickel-based single crystal superalloy, which contained Nickel (Ni), cobalt (Co), aluminum (Al), chromium (Cr), molybdenum (Mo), tantalum (Ta), tungsten (W), rhenium (Re), ruthenium (Ru), etc. The chemical composition is summarized in Table 1. The crystal orientation of the cast rods was determined by X-Ray diffraction (X-Ray Laue Diffraction Systems, Photonic Science Limited, East Sussex, UK). The results show that all bars selected for the LCF tests were within 10° deviations of the [001] crystallographic direction. The typical three-step heat procedures, including an elevated temperature solid solution treatment at 1340 °C followed by two aging treatments at 1100 °C and 870 °C in argon and vacuum, were performed to process the casting material. Air cooling was applied after each heat process. Low cycle fatigue specimens (5.5 mm in diameter of gauge and 76 mm in length) were machined and polished from completely heat-treated SC bars before test.

Table 1. Nominal composition of the experimental alloy (wt%).

| Al + Ta	Co + Cr	Mo + W	Re + Ru	Ni
12%	8%	9%	7.5%	Bal.%

The LCF tests were all conducted with an MTS servo machine (MTS-100kN-10, MTS, Eden Prairie, MN, USA) and were carried out in air at 900 °C and 980 °C under fully reversed ($R = -1$) total strain control according to the standard "GB/T 15248-2008" [23]. The strain amplitudes ($\Delta\varepsilon_t/2$) were 0.8% with a triangle waveform and a constant strain rate of $5 \times 10^{-3} s^{-1}$ at both temperatures. The samples were kept warm for 30 min before the fatigue test. The equipment used for heating was a Model 652.02 high temperature furnace (MTS-100kN-10, MTS, Eden Prairie, MN, USA). After the fatigue test, the site of crack initiation and the path of crack propagation were observed by scanning electron microscopy (SEM, FEI Quanta 650, FEI, Portland, OR, USA). Additionally, the 3D morphology of the fatigue fractures were measured by 3D measurement laser microscopy (OLS4100-SAF, Olympus, Japan). The chemical compositions of the oxidation microcracks were determined by energy dispersive spectroscopy (EDS, Oxford, UK) under SEM, and the

oxidation microcrack was observed in longitudinal sections of 3 mm from the fracture surface. The diffusivity of the metallic elements was simulated using Thermo-Calc software (Thermo Calc 2022a, Thermo-Calc Software AB (2022.1.95234-411), Stockholm, Sweden).

3. Results and Discussion

3.1. Cyclic Stress Amplitude and Cycle Time

The cycle times (N_f) of the alloy at 900 °C and 980 °C were 3028 and 1287 cycles, which convert to 5.4 h and 2.1 h, respectively. The cyclic stress amplitudes were taken as the average of the stress amplitudes (half the stress range) for cycles $N_f/2 - 1$, $N_f/2$ and $N_f/2 + 1$. Figure 1 shows the cyclic stress amplitude and cycle time of the alloys tested at 900 °C and 980 °C. The cyclic stress amplitude and cycle life of the alloy at 900 °C are significantly higher than that at 980 °C.
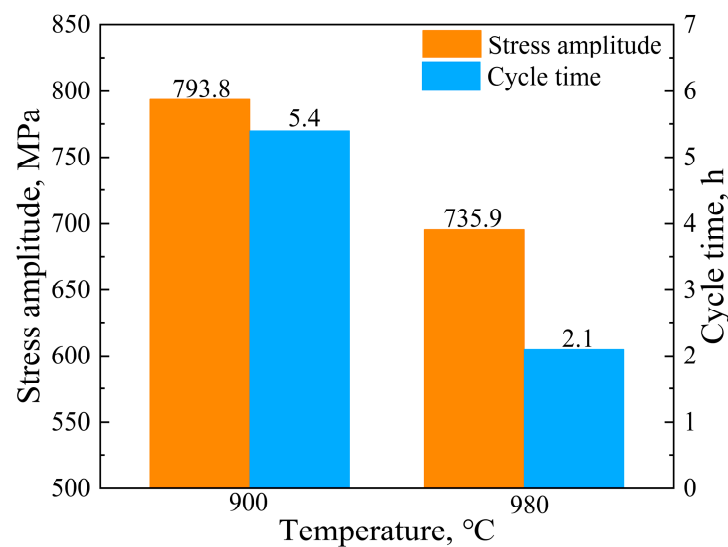
Figure 1. Cyclic stress and cycle time of alloys at different temperatures during LCF.

3.2. Initiation and Propagation of Main Cracks

Figure 2 shows the initiation and propagation of low-cycle fatigue cracks in the alloy at different temperatures. The crack initiation locations are close to the surface for both temperatures; the crack initiation locations are shown by dashed red boxes and white arrows. At 900 °C, the crack originates at the micropore on the subsurface, shows obvious circular traces around the micropore, and then expands slowly on the {001} plane. After a certain distance, it expands rapidly on multiple {111} planes until fracture. At 980 °C, crack initiation occurs at the surface oxidation and presents a semicircular trace, then spreads slowly on the {001} surface. After spreading a lengthy distance, it transitions into other planes. The areas with the same color in Figure 2a and c indicate the same height, which is the {001} plane. At 900 °C, crack growth occupies a large proportion of the {111} plane, indicating that the dislocation has a weak ability to bypass the γ' phase at this temperature; the alloy deformation requires the dislocation to cut through the γ' phase, as shown in Figure 2a,b. At 980 °C, however, crack growth mainly occurs on the {001} plane, indicating that the dislocation mainly moves in the matrix channel and can bypass the γ' phase. As a result, the cyclic stress at 900 °C is significantly higher than at 980 °C, as shown in Figure 2c,d. At 900 °C, higher cyclic stress can promote the initiation of cracks on the subsurface of the micropore and reach the critical crack length faster than the oxidation crack, which is one of the reasons for the main crack initiating at the subsurface defect.
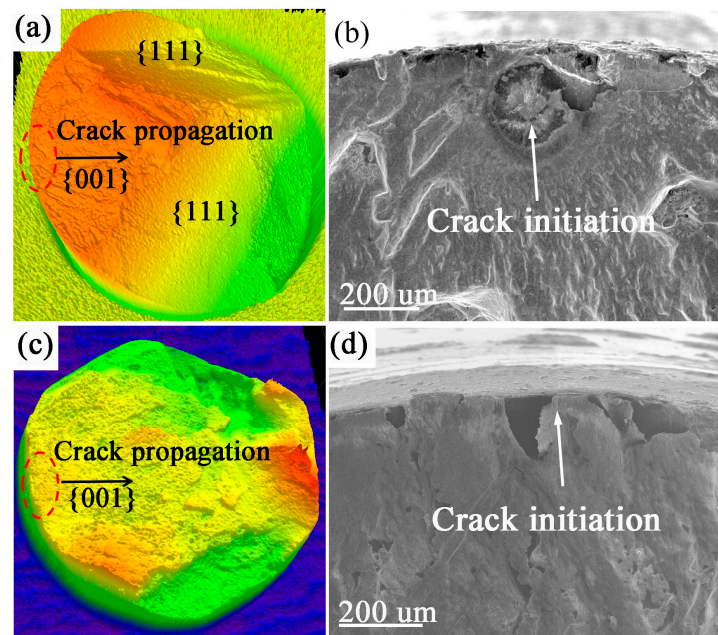
Figure 2. Low cycle fatigue crack initiation at different temperatures: (**a**,**b**) 900 °C and (**c**,**d**) 980 °C. The 3D images in (**a**,**b**) were taken with a 3D measurement laser microscopy.

Figure 3 shows the oxidation crack growth of the alloy after low-cycle fatigue at different temperatures. At 900 °C (Figure 3a) and 980 °C (Figure 3b), a certain thickness of oxide layer is generated on the surface of the sample. The oxide layer close to the oxidizing environment has cracks and tends to spall. A portion of the oxide layer grows faster and extends inward in a direction perpendicular to the applied stress axis and consistent with the direction of propagation of the main crack shown in Figure 2. Meanwhile, at 900 °C, the oxidation layer forms microcracks about 45° in the direction of the main crack growth, while at 980 °C the microcrack formation direction is parallel to the main crack growth direction and the microcrack initiation is in the center of the oxidation layer.
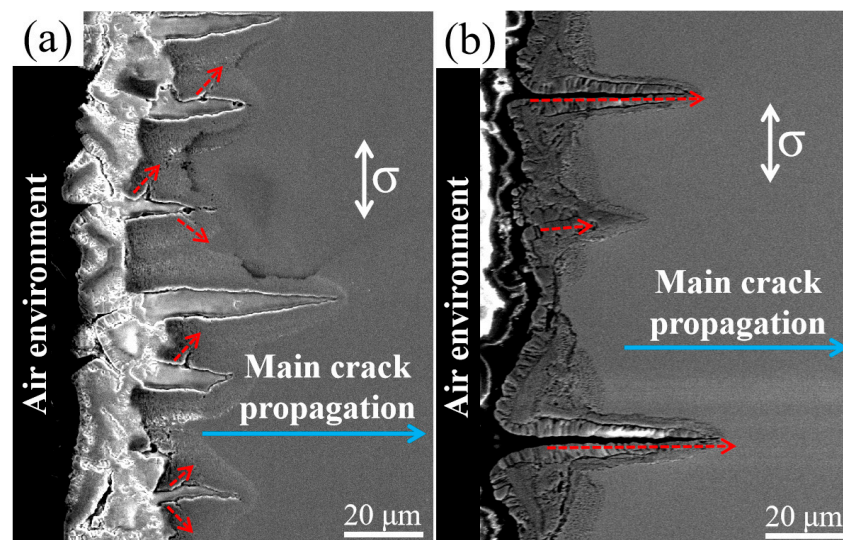
Figure 3. Surface oxidation layer of alloy after low cycle fatigue at different temperatures: (**a**) 900 °C and (**b**) 980 °C.

3.3. Oxidation-Induced Cracks

Figure 4 shows the surface oxide layer of the alloy after low cycle fatigue at 900 °C. The surface oxide layer of the alloy can be divided into two layers, namely, the outer oxide layer and the inner oxide layer. The outer oxide layer is dominated by Ni and Co oxides, and more microscopic cracks are produced inside. The inner oxide layer can be divided into three layers according to the element composition, which are: ① the Al oxide layer; ② the Al, Cr, Mo oxide layer; and ③ the Al and Cr oxide layer. From the distribution of oxygen elements, there is no significant reduction of oxygen atoms at the interface between the outer oxide layer and the inner oxide layer, indicating that there is no cleavage at the outer/inner oxide layer interface. The enrichment degree of Al and O (oxygen) decreases from left to right, indicating that the diffusion ability of O^{2-} decreases with the increase in depth. There is no obvious depletion of Al in the right region of oxide layer ①, and the γ and γ' phases remain in a coherent state. Al is an element-forming γ' phase, and the thermal stability of the oxide layer is higher than that of the γ' phase. Broadly, the disappearance of Al indicates the decomposition of the γ' phase driven by the element concentration gradient [24,25]. Therefore, there is no obvious depletion zone of the γ' phase in the oxide layer at 900 °C.
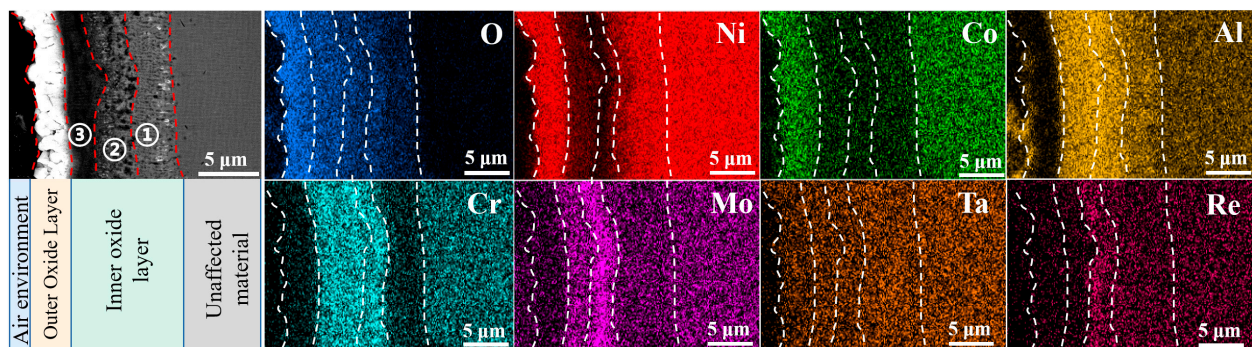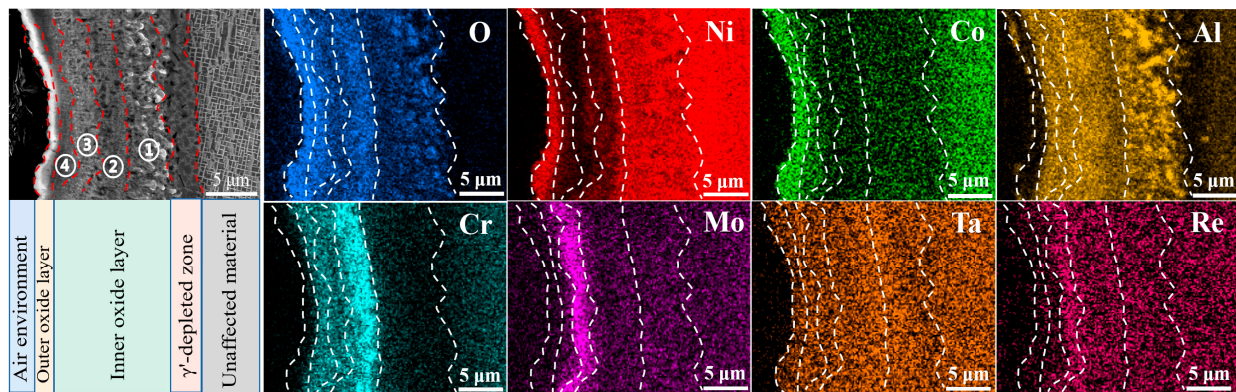

Figure 4. SEM-EDS maps of the surface oxide layer after fatigue at 900 °C.

Figure 5 shows the surface oxide layer of the alloy after low cycle fatigue at 980 °C. The oxide layer of the alloy is divided into three layers, namely, the outer oxide layer, the inner oxide layer, and the γ'-depleted zone. The outer oxide layer is composed of Ni and Co oxides, forming a few cracks. From the distribution of oxygen elements, there is no crack at the outer/inner oxide layer interface. The inner oxide layer can divide into four layers according to the element composition, which are ① the Al oxide layer; ② the Al, Cr oxide layer; ③ the Al, Cr, Mo oxide layer; and ④ the Al, Cr, Co oxide layer. The oxide of Al in superalloys at high temperatures is usually Al_2O_3 [17,26]. The size of Al_2O_3 in layer ① is large and the oxide layer is discontinuous, which is conducive to accelerating the oxygen atom transport and promoting the rapid growth of the oxide layer. As a result, the oxide layer forms a bulge into the interior of the alloy, and it is commonly assumed that this bulge grows faster than the remaining regions, gradually developing into the inward extending oxide layer shown in Figure 3 [24,27,28]. There is an obvious Al depletion region on the right side of oxide layer ① and the shape of the γ' phase disappears, indicating that there is a γ'-depleted zone. The presence of the γ' phase is the main strengthening mechanism of nickel-based single crystals; thus, its disappearance reduces the fatigue resistance of the alloy, which is conducive to crack growth.
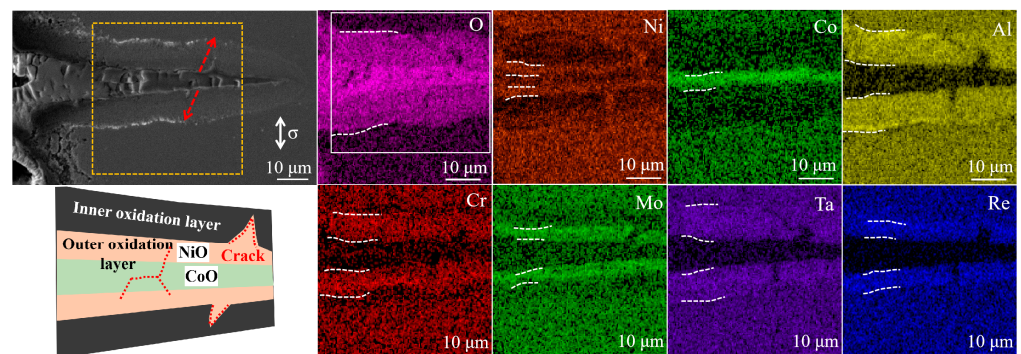
Figure 5. SEM-EDS maps of the surface oxide layer after fatigue at 980 °C.

The stratification of the oxide layer is the result of the growth of the oxide layer driven by the charge gradient [29–32]. The oxidation of alloys at high temperatures proceeds as follows. Oxygen molecules are adsorbed onto the sample surface; Al and Cr formed from oxides with low Gibbs free energy are first oxidized, especially Al with high content. Al_2O_3 nucleates on the alloy surface and gradually forms a continuous dense Al_2O_3 layer. Because the diffusion rate of Al^{3+} in the Al_2O_3 layer is lower than that of O^{2-}, the growth of the oxide layer mainly depends on the internal diffusion of O^{2-} to react with Al^{3+} in order to form a fresh Al_2O_3 oxide layer; thus, the oxide layer of Al gradually grows inward [31,33]. The oxidation process of elements such as Ni and Co is mainly driven by the outward diffusion of metal cations, which diffuse to the oxide layer/air interface and react to form oxides in oxygen. Therefore, the oxide layer of Ni and Co grows outward from the oxide layer of Al and finally forms the outer oxide layer [32]. Heavy metal elements such as Mo are typically distributed near the interface between the inner and outer oxide layers due to their slow outward diffusion. Because Cr is prone to oxidation and has a fast outward diffusion rate, its distribution is broad and usually distributed near the interface between the outer oxide layer and the inner oxide layer. The outward diffusion rate of Ta and Re is slow, usually distributed near the interface; due to the short high-temperature oxidation time, the oxidation layer of Ta and Re is not apparent in the absence of cracks to transport oxygen. At 980 °C (Figure 5), the diffusion ability of O^{2-} is stronger, the formed Al_2O_3 grows rapidly, and the Al is consumed rapidly, resulting in a less dense inner Al oxide layer with different thickness along with the formation of a γ'-depleted zone [26,34]. Based on the sample composition, the diffusion coefficients of different metallic elements in the alloy were simulated using the Thermo-Calc software (2022.1.95234-411); the results are shown in Figure 6. It can be seen that Al and Cr have significant negative diffusion coefficients, while Ni and Co have significant positive diffusion coefficients. Thus, Al and Cr are the dominant metallic elements in the inner oxide layer, while Ni and Co are the dominant metallic elements in the outer oxide layer. As the temperature increases, the diffusivity of the alloyed elements increases, most significantly for Ni.
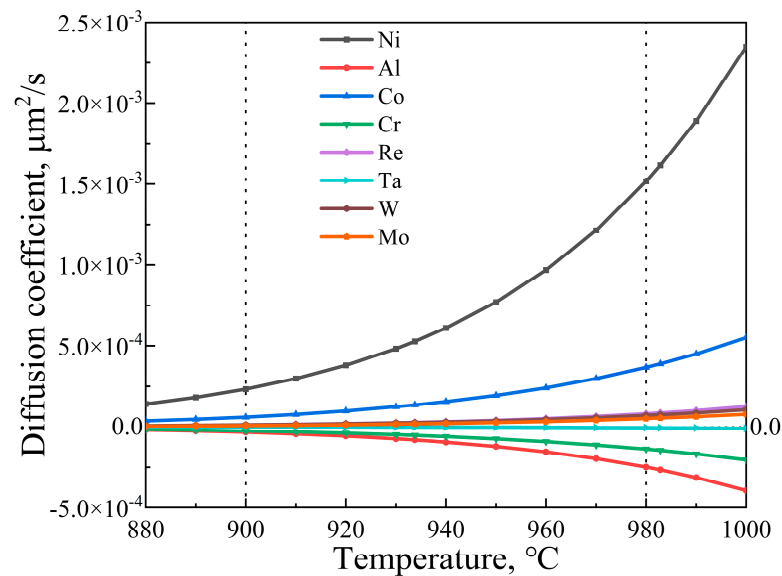
Figure 6. Diffusion coefficients for different metallic elements in the alloy.

Figure 7 shows the EDS image of oxidation cracks of the alloy after low cycle fatigue at 900 °C. The region shown by the yellow dashed box is the EDS analysis region, the red dashed arrow shows the direction of the initiation of microcracks in the oxide layer, and the white dashed line marks the width range of each metallic oxide in Figure 7. At 900 °C, the outer oxide layer is formed with Ni and Co as the main metal elements, while the inner oxide layer is represented by Al, Cr, and other metal elements. While a small number of microscopic cracks appear in the outer oxide layer, there are no significant cracks at the interface of the outer/inner oxide layer. Two obvious cracks appear in the inner oxide layer, about 45° in the direction of the stress axis, and the gap where the cracks appear is filled by the outer oxide layer, indicating that the cracks did not appear during the cooling process with a short high temperature time. It is worth noting that the distribution area of Ni and Co in the inner oxide layer is mainly not coincident, forming an Ni oxide layer close to the inner oxide layer and a Co oxide layer further away from the inner oxide layer. Generally, this oxide layer contains only Ni or Co and is formed in NiO or CoO [26,35]. According to the analysis of Ellingham's figure [36,37], at the same temperature, the partial pressure of oxygen formed by Co is smaller and the diffusion rate of Co is slightly faster than that of Ni. In this case of O^{2-} deficiency, it is likely that the oxide layer of Co is closer to the outside than that of Ni. While there are microcracks in the surface oxide layer, they do not continue to propagate inward. The lower left corner of Figure 7 shows the oxide layer and crack distribution at 900 °C.

Figure 7. SEM-EDS maps of the oxidation cracks after fatigue at 900 °C.

As shown in Figure 8, at 980 °C, an outer oxide layer is formed with Ni and Co as the main metal elements along with an inner oxide layer represented by Al, Cr, and other metal elements. Long cracks appear in the outer oxide layer parallel to the direction of propagation of the main crack, while additional cracks appear in the outer oxide layer and at the interface between the outer and inner oxide layers. At 980 °C the diffusion capacity of O^{2-} is strong, and the increase of diffusion coefficient of Ni is considerably higher than that of Co (as shown in Figure 6). Thus, oxidation of Ni and Co is not significantly different, most of the distribution areas of Ni and Co in the inner oxidation layer coincide, and Ni and Co can form a solid solution. It is widely believed that the oxide layer where Ni and Co exist at the same time is mainly (Ni,Co)O, and includes parts of NiO or CoO [26,33]. The diagram at the lower left corner of Figure 8 shows the oxide layer and crack distribution at 980 °C.
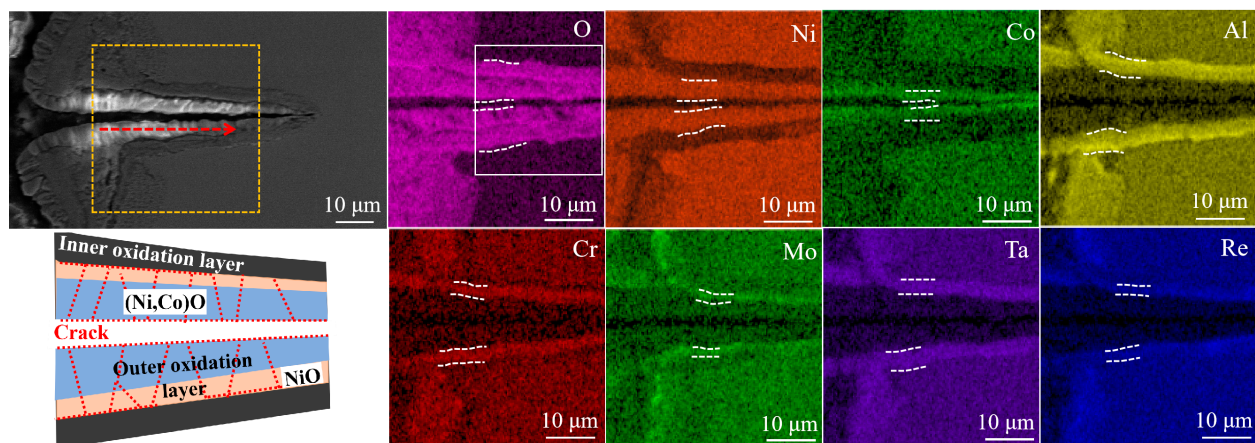

Figure 8. SEM-EDS maps of the oxidation cracks after fatigue at 980 °C.

There are two main mechanisms for the cracking of the surface oxide layer [27,38]. First, the fracture resistance of the oxide layer/matrix interface is higher than that of the oxide layer itself, in which case the internal stress in the oxide layer causes shear fracture of the oxide layer, then the fractured oxide layer causes local spalling. Second, the interface strength is lower than the fracture resistance of the oxide layer. In this case, the interface first creates microcracks; as these micro-racks are connected to each other, long cracks form the oxide layer becomes separated from the matrix, and finally the oxide layer begins to spall. One of the reasons for the formation of interfacial cracks is the consumption of Al. The absence of Al near the oxide layer leads to the formation of vacancies; the accumulation of vacancies forms holes and pores at the interface, and cracks gradually start at the interface between the oxide layer and the matrix. After the formation of an interfacial microcrack, the spacing between the oxide layer and the matrix on either side of the microcrack increases; this portion of the oxide layer produces partial warping, and cracks are more likely to occur under external cyclic stress. At the same time, thicker oxide layers are prone to cracking due to their large compressive stress and difficult deformation. These two mechanisms occur mainly in long-term oxidation environments with no or low applied stress. In this study, the stress was elevated and the oxidation time was short, which requires a fresh interpretation of the growth of surface oxidation cracks.

To analyze the cause of the cracks in the oxide layer, the widths of each metal oxide layer shown in Figures 7 and 8 and their fraction in the total oxide layer were statistically analyzed. The statistical range is shown within the white wire frame of the distribution map of O, and the statistical results are shown in Figure 9. At 900 °C, the oxide width and proportion of Al, Cr, Mo, Ta, and Re in the total oxide layer are significantly higher than that at 980 °C. At 980 °C, the width of Ni and Co oxide layers and the proportion of the total oxide layer are higher, especially the Ni oxide layer. It is worth noting that it is difficult to calculate the content of metal oxides in the oxide layer for the following reasons. (1) Unlike

the long-term thermal exposure study, the oxidation time in this study was short, making it difficult for all the oxide layers to become dense and uniform metal oxides. (2) With the initiation of microcracks in the oxide layer, the oxidation time from the surface of the sample to the inside of the matrix and the content of metal oxides are different. (3) The oxide layers of various metal elements overlap and are difficult to distinguish accurately. The width of the oxide layer can represent the range of metal oxides, and there is a concentration gradient in the metal oxides content of the oxide layer. In general, the stronger the ability to form metal oxides, the wider the range of the metal oxides distribution; hence, the width of the oxide layer can be used to roughly characterize the metal oxides content. Of course, this can only be used as a simple proof, not as an exact computational basis.
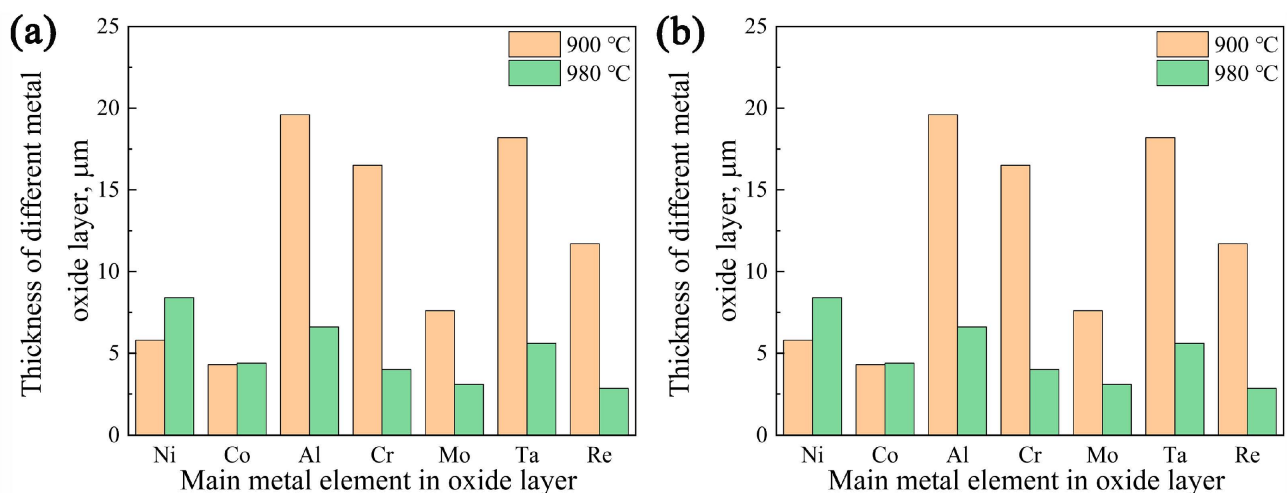

Figure 9. Oxidation of different metals at 900 °C and 980 °C: (**a**) metal oxide thickness and (**b**) the proportion of metal oxide layers to the total oxide layer.

There are two main stresses that cause oxidation layer spalling and cracking due to oxidation layer accumulation, namely, thermal stress and growth stress [39,40]. The difference in the thermal expansion coefficient between different oxide layers or between the oxide layer and matrix leads to the generation of thermal stress [25,41,42]. Due to the difference in the coefficient of thermal expansion, the thermal stress accumulates as the oxide layer and the matrix are heated and cooled due to their different simultaneous expansion and contraction. Because the low-cycle fatigue test of the alloy was performed at a constant temperature, the initiation and expansion of oxide cracks during low-cycle fatigue at constant temperature was independent of thermal stress. When certain metal elements are oxidized, the volume of the resulting oxide becomes larger than the volume of the metal element, resulting in the accumulation of growth stress in the oxide layer. Pilling and Bedworth et al. [27,43] proposed that the ratio of the volume of the generated oxide to the volume of the original metal element is used to react the density of the oxide layer, that is, the PBR (Pilling–Bedworth Ratio). The larger the PBR, the denser the resulting oxide layer and the greater the compressive stress accumulated in the oxide layer. The PBR of some oxides is [44,45]: $1.28Al_2O_3$-$1.65NiO$-$1.86CoO$-$1.87WO_2$-$2.07Cr_2O_3$-$2.16ReO_2$-$2.5Ta_2O_5$-$3.27MoO_3$. It can be seen from Figures 7–9 that the width of Al, W, Cr, Re, Ta, and Mo in the inner oxide layer is significantly higher at 900 °C than at 980 °C; thus, the inner oxide layer generates greater compressive stress at 900 °C. The actual inner oxide layer has a certain slope due to the thicker portion of the inner oxide extending closer to the sample surface. The internal compressive stress is not on the same level. In addition, due to the presence of the external stress, the oxide layer produces a certain degree of bending, which exacerbates the bias of the internal compressive stress. Therefore, cracks can easily occur in the inner oxide layer when the internal compressive stress exceeds the fracture strength of the inner oxide layer. In the outer oxide layer, at 900 °C, the oxide layer of Ni and Co is

separated and the oxide layer of Ni and Co is thinner, meaning that the compressive stress formed inside the oxide layer of Ni and Co is smaller. At 980 °C, the Ni and Co oxide layers overlap, indicating that a thicker (Ni,Co)O oxide layer is formed; the BPR value of this layer is about 1.65~1.86 [44,45]. Moreover, (Ni,Co)O tends to form hexagonal structures, and the binding force at the interface of the different (Ni,Co)O is weak [17]. Thus, it can easily crack at the outer oxide layer at 980 °C.

Figure 10 shows the morphology of the oxide layer after low-cycle fatigue at 980 °C, in which Figure 10b is the enlarged image of the local region in Figure 10a. Continuous cracks appear inside the outer oxide layer, at the interface between the outer oxide layer and the inner oxide layer, and even extend to the crack tip. The red dashed line in Figure 10 shows the main direction of the crack. Along with the progress of the crack, branch cracks allow the interface of the different (Ni,Co)O to appear continuously, propagating from the interface to the oxide layer or from the oxide layer to the interface, as indicated by the white dashed lines. As the cycle time increases, the cracks grow simultaneously along the interface and the outer oxide layer and the two propagation paths promote each other. With the expansion of the branches, two situations may occur. First, it is more convenient to transport oxygen along the crack channel to the crack tip, promoting the oxidation and embrittlement of the crack tip region and leading to crack growth. Second, with the increase of cracks in the oxide layer, the probability of spalling of the oxide layer increases. This causes the crack length and opening angle in the oxide layer and at the interface to increase, in turn increasing the driving force of crack growth. Consequently, cracks in the outer oxide layer and cracks in the inner/outer interface promote each other and expand together. It is worth mentioning that there is an obvious γ′-depleted zone near the inner oxide layer, which is the result of rapid O^{2-} transport caused by the cracks.
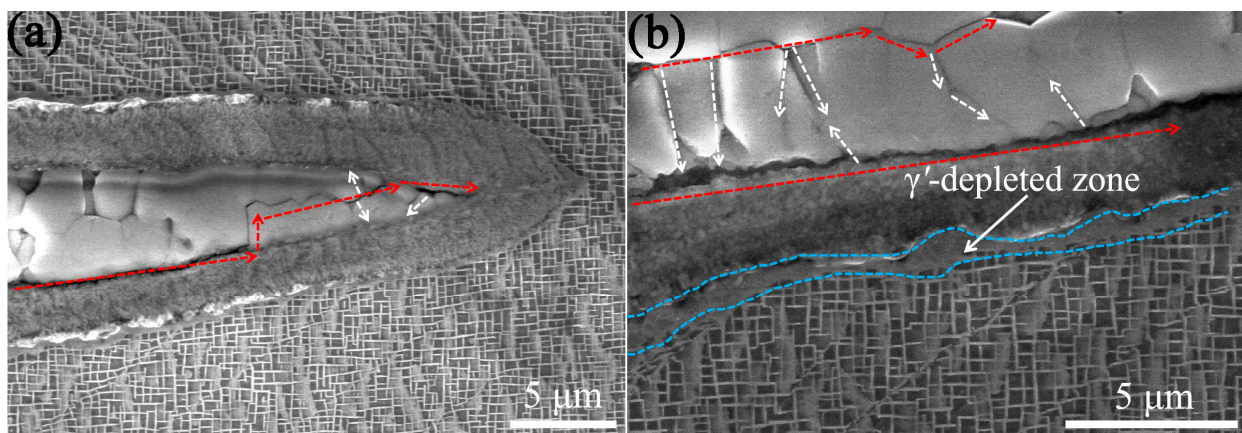

Figure 10. Morphology of the oxide layer after low-cycle fatigue at 980 °C: (**a**) the part that enters the matrix and (**b**) enlarged view of areas in (**a**).

The presence of cracks in the oxide layer and at the inner/outer oxide layer interface significantly affects the crack tip growth rate. Figure 11 shows the EDS map analysis of the alloy fatigue–oxidation crack tip regions at 900 °C. From the distribution of oxygen elements, the enrichment degree of oxygen elements in the outer oxide layer is obviously higher than that in the inner oxide layer. As shown in the distribution of Al elements, there is no Al barren zone.
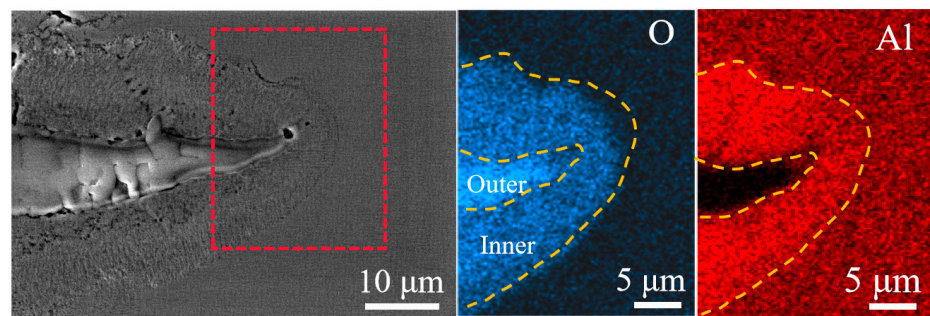
Figure 11. SEM-EDS maps of the crack tip oxidation after fatigue at 900 °C.

Figure 12 shows the EDS map analysis of the fatigue-oxidation crack tip regions at 980 °C. The enrichment degree of oxygen elements in the outer oxide layer is basically the same as that in the inner oxide layer. The results show that the oxygen at crack tip is more abundant at 980 °C, and the diffusion ability of O^{2-} to the interior is stronger. From the distribution of Al elements, there is an obvious Al barren zone (shown by the dotted white line) on the right side of the inner oxide layer. The results show that the oxidation rate of the crack tip is rapid at 980 °C; the rapid consumption of Al element forms a large Al^{3+} concentration gradient, the γ' phase dissolves, and then a γ'-depleted zone appears.
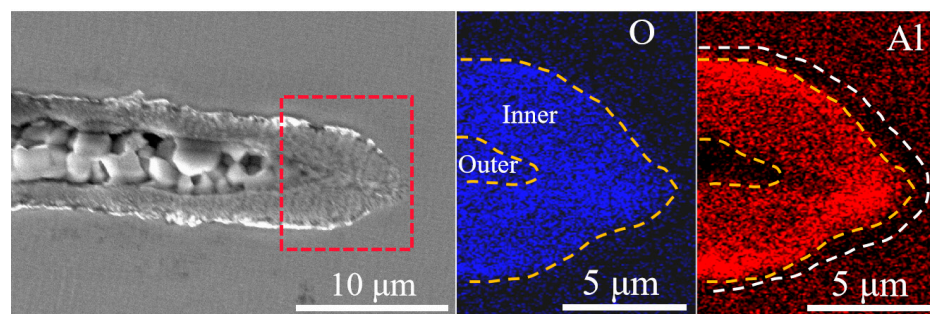
Figure 12. SEM-EDS maps of the crack tip oxidation after fatigue at 980 °C.

Compared with the size of the oxide layer, the thickness of the oxide layer at the crack tip at 980 °C (Figure 12) is significantly less than that at 900 °C (Figure 11), indicating that the growth rate of the crack is faster at 980 °C and the residence time in the same length is shorter. In general, the growth rate of the oxidation crack tip at 980 °C is significantly higher than that at 900 °C, which is an essential reason for the oxidation crack length at 980 °C quickly reaching the critical crack length and eventually becoming the main crack.
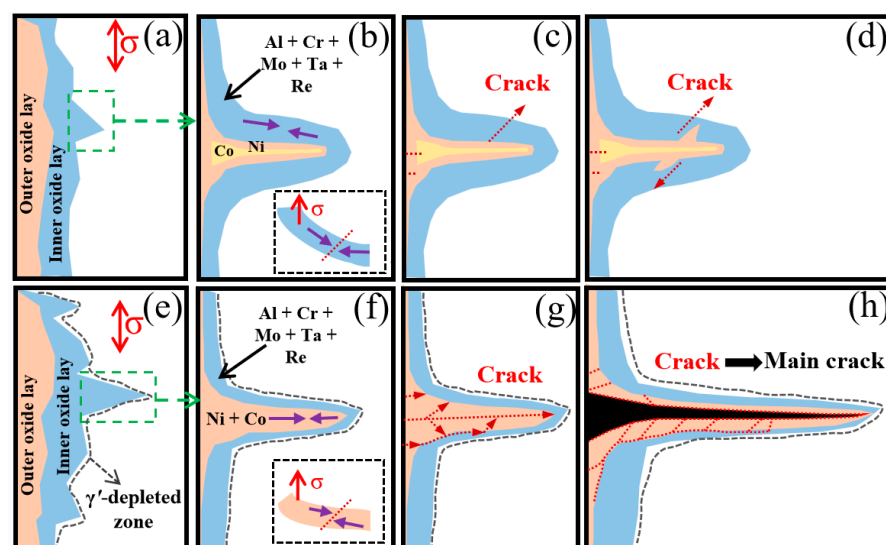
3.4. Initiation and Propagation of Oxidation Cracks

Figure 13 shows the initiation and propagation process of oxidation cracks at different temperatures, which can be divided into the following four main steps:

(1) After oxygen molecules are absorbed on the surface of the alloy, O^{2-} and Al^{3+} diffuse internally while other metal ions such as Ni^{2+} and Co^{2+} diffuse towards the surface, gradually forming an inner oxide layer and an outer oxide layer with different depth distances on the surface (shown in Figure 13a,e). At the high temperature of 980 °C, the γ' phase in the adjacent region dissolves and forms the γ'-depleted zone due to the rapid depletion rate of Al^{3+}.

(2) With the development of oxidation layer penetration into the matrix, stress concentration at the tip of the oxide layer promotes the inward growth of the oxide layer [12]. The fatigue resistance of the γ'-depleted zone is lower than that of the matrix, meaning that the resistance of crack expansion at 980 °C is smaller and the expansion rate is faster. At 900 °C, the expansion rate of the oxide layer is low, the thickness of the inner oxide layer is large, and the internal compressive stress is generated. There is a certain

angle between the inner oxide layer and the horizontal line, and the large external cyclic stress causes the inner oxide layer to bend to a certain extent; thus, the internal compressive stress is not on the same horizontal line. Shear fracture may occur when the compressive stress exceeds the shear strength of the inner layer. At 980 °C, the thickness of the inner oxide layer is narrow and the thickness of the outer oxide layer is large, meaning that it is easy for cracks to form in the outer oxide layer under the action of internal compressive stress. This step is illustrated in Figure 13b,f.

(3) At 900 °C, with the growth of cracks in the inner oxide layer, the internal stress in the oxide layer is released and the outer oxide layer gradually fills the cracked area of the inner oxide layer. As the surface oxide layer thickens, microcracks perpendicular to the stress axis are gradually created in the surface oxide layer and expand inward under self-compressive stress and external cyclic stress. Because the outer oxide layer deep in the matrix is divided into two layers and the thickness of each layer is very small, the internal compressive stress in the outer oxide layer is significantly reduced, and it is difficult for the surface microcracks to continue to expand in the outer oxide layer. The surface crack is not connected to the crack initiation in the inner oxide layer and the opportunity for rapid oxygen delivery and rapid crack propagation is lost. At 980 °C, when the microcrack from the surface oxide layer expands internally, it is easy to connect with the microcrack already existing in the (Ni,Co)O oxide layer, allowing a lengthy crack to form or expand along the inner/outer oxide layer interface. This allows oxygen a rapid expansion channel and provides the microcrack with a larger opening angle, meaning that the crack can expand rapidly. The crack in the oxide layer and the crack at the oxide layer interface grow forward and branch into more fragile regions, finally achieving the mutual promotion of the crack in the oxide layer and the crack at the oxide layer interface, thereby accelerating crack propagation. This step is illustrated in Figure 13c,g.

(4) At 900 °C, the growth rate of the cracks induced by oxidation is slow. At the same time, the higher cyclic stress level leads to crack initiation at the subsurface defect and faster growth to the critical crack length, meaning that the final oxidized crack does not become the dominant main crack. At 980 °C, the crack initiation caused by oxidation has a rapid growth rate, while the crack initiation at the internal or subsurface defect is late under low cyclic stress and the growth rate is slow. Thus the oxidation crack becomes the main crack. This step is illustrated in Figure 13d,h.

Figure 13. Schematic diagram of initiation and propagation of oxidation cracks at different temperatures: (**a**–**d**) 900 °C and (**e**–**h**) 980 °C.

4. Conclusions

The crack initiation behaviors of a single crystal superalloy with the [001] orientation under low-cycle fatigue–oxidation conditions have been systematically investigated with SEM at 900 °C and 980 °C, and the variation of oxidation and crack initiation mechanisms has been proposed. In addition, the effect of temperature on oxidation and crack initiation have been analyzed in detail. The main conclusions are as follows:

(1) Under the same conditions, the cyclic stress and cycle life of low cycle fatigue at 900 °C are higher than that at 980 °C. Main crack initiation occurs near the surface defect at 900 °C, while at 980 °C main crack initiation occurs at the surface oxide layer.

(2) At 900 °C, the rate of oxidation and metal cation diffusion are low, the crack propagation rate is slow, and the inner oxide layer is thick, while the outer oxide layer is thin in the oxidation zone deep into the matrix. Although compressive stresses accumulated by the thicker inner oxide layer create microcracks, these microcracks have difficulty connecting to surface microcracks and forming rapid oxygen transport channels, which is an essential reason for the cracks growing slowly and not developing into main cracks.

(3) At 980 °C, the rate of oxidation and metal cation diffusion are fast, the formation of a γ'-depleted zone promotes crack propagation, and the inner oxide layer is thin, while the outer oxide layer is thick in the oxidation zone deep into the matrix. Microcracks form in the outer oxide layer and quickly connect to microcracks at the surface and the inner/outer oxide layer interface, which then grow into long cracks that become channels for rapid oxygen transport, accelerating the crack growth rate. Eventually, the oxide cracks become main cracks.

Currently, there are few studies on the effect of oxidation on the propagation pattern of fatigue crack initiation in nickel-based single crystals under cyclic load. In our work, the samples were cyclically broken, meaning that the cycle times were not the same. Further in-depth comparison and analysis of the effect of oxidation on crack initiation could be facilitated by discontinuities in the same cycle and by the choice of additional stress levels.

Author Contributions: P.W.: Conceptualization, data curation, formal analysis, investigation, writing—original draft preparation; X.Z.: Conceptualization, resources, writing—review and editing, supervision, funding acquisition; Q.Y.: methodology, investigation, resources, project administration; W.X.: methodology, project administration, writing—review and editing; Q.D.: validation, project administration, visualization; H.B.: methodology, project administration, visualization; Y.G.: resources, supervision, writing—review and editing; Z.Z.: resources, project administration, supervision. All authors have read and agreed to the published version of the manuscript.

Data Availability Statement: The data that support the findings of this study are available from the corresponding author, upon reasonable request.

Conflicts of Interest: The authors declare no conflict of interest.

References

1. Reed, R.C. *The Superalloys: Fundamentals and Applications*, 1st ed.; Cambridge University Press: Cambridge, UK, 2006.
2. Boyce, M.P. *Gas Turbine Engineering Handbook*, 4th ed.; Butterworth-Heinemann Press: Oxford, UK, 2012.
3. GoBel, M.; Rahmel, A.; Schütze, M. The isothermal-oxidation behavior of several nickel-base single-crystal superalloys with and without coatings. *Oxid. Met.* **1993**, *39*, 231–261. [CrossRef]

4. Narita, T.; Thosin, K.Z.; Fengqun, L. Development of re-based diffusion barrier coatings on nickel based superalloys. *Mater. Corros.* **2015**, *56*, 923–929. [CrossRef]

5. Cowles, B.A. High cycle fatigue in aircraft gas turbines—An industry perspective. *Int. J. Fract.* **1996**, *80*, 147–163. [CrossRef]

6. Sun, B.; Zhang, T.; Song, L.; Zhang, L. Oxidation behavior in static air and its effect on tensile properties of a powder metallurgy EP962NP nickel-based superalloy. *J. Alloys Compd.* **2022**, *934*, 167795. [CrossRef]

7. Carter, T.J. Common failures in gas turbine blades. *Eng. Fail. Anal.* **2005**, *12*, 237–247. [CrossRef]

8. Zhang, T.; Yuan, H. Stress shielding in laser melting multilayered nickel-base superalloys under monotonic and cyclic loadings. *Int. J. Fatigue* **2023**, *167*, 107349.1–107349.14. [CrossRef]

9. Yuan, S.H.; Wang, Y.R.; Wei, D.S. Experimental investigation on low cycle fatigue and fracture behaviour of a notched Ni-based superalloy at elevated temperature. *Fatigue Fract. Eng. Mater. Struct.* **2014**, *37*, 1002–1012. [CrossRef]

10. Perepezko, J.H. The hotter the engine, the better. *Science* **2009**, *326*, 1068–1069. [CrossRef]

11. MacLachlan, D.W.; Knowles, D.M. Fatigue behaviour and lifing of two single crystal superalloys. *Fatigue Fract. Eng. Mater. Struct.* **2001**, *24*, 503–521. [CrossRef]

12. Murray, S.P.; Cervellon, A.; Cormier, J. Low cycle fatigue of a single crystal CoNi-base superalloy. *Mater. Sci. Eng. A* **2021**, *827*, 142007. [CrossRef]

13. Li, W.Q.; Zhao, X.B.; Cheng, Y. Effect of molybdenum on cyclic oxidation behavior of 4th generation nickel-based single crystal superalloys. *Corros. Sci.* **2023**, *81*, 345–356. [CrossRef]

14. Syed, A.U.; Martinez, F.D.; Roberts, T. Performance Comparison Between Isothermal Hot Corrosion And In Situ Cyclic Hot Corrosion of Nickel-Based Superalloys. *Oxid. Met.* **2021**, *96*, 43–55. [CrossRef]

15. Jia, Y.X.; Zhu, S.L.; Zhang, K. Improving the oxidation behavior of low expansion Ni+CrAlYNO coating systems by regulating the oxygen content. *Corros. Sci.* **2021**, *189*, 109582.1–109582.13. [CrossRef]

16. Liu, L.; Meng, J.; Liu, J.L. Effects of crystal orientations on the low-cycle fatigue of a single-crystal nickel-based superalloy at 980 °C. *Acta Metall. Sin.* **2019**, *32*, 381–390. [CrossRef]

17. Pei, H.; Wen, Z. Oxidation behavior and mechanism of a ni-based single crystal superalloy with single α-Al_2O_3 film at 1000 °C. *Appl. Surf. Sci.* **2017**, *411*, 124–135. [CrossRef]

18. Hong, H.U.; Choi, B.G.; Kim, I.S. Characterization of deformation mechanisms during low cycle fatigue of a single crystal nickel-based superalloy. *J. Mater. Sci.* **2011**, *46*, 5245–5251. [CrossRef]

19. Fleury, E.; Rémy, L. Low cycle fatigue damage in nickel-base superalloy single crystals at elevated temperature. *Mater. Sci. Eng. A* **1993**, *167*, 23–30. [CrossRef]

20. Anton, D.L. Low cycle fatigue characteristics of <001> and randomly aligned superalloy single crystals. *Acta Metall.* **1984**, *32*, 1669–1679. [CrossRef]

21. Golubovskiy, E.R.; Svetlov, I.L.; Petrushin, N.V. Low-cycle fatigue of nickel superalloy single crystals at elevated temperatures. *Russ. Metall. (Met.)* **2010**, *2010*, 941–947. [CrossRef]

22. Gabb, T.P. Orientation and temperature dependence of some mechanical properties of the single-crystal nickel-base superalloy René N4: Part II. Low cycle fatigue behavior. *Metall. Trans. A* **1986**, *17*, 497–505. [CrossRef]

23. *GB 15248-2008*; The Test Method for Axial Loading Constant-Amplitude Low-Cycle Fatigue of Metallic Materials. Standards Press of China: Beijing, China, 2008. (In Chinese)

24. Zhao, Z.; Li, Q. Transition from internal to surface crack initiation of a single-crystal superalloy in the very-high-cycle fatigue regime at 1100 °C. *Int. J. Fatigue* **2021**, *150*, 106343. [CrossRef]

25. Pfennig, A.; Fedelich, B. Oxidation of single crystal PWA 1483 at 950 °C in flowing air. *Corros. Sci.* **2008**, *50*, 2484–2492. [CrossRef]

26. Li, W.Q.; Zhao, X.B. Effect of elements distribution on oxidation behavior of a nickel-based single crystal superalloy. *Vacuum* **2023**, *209*, 111780. [CrossRef]

27. Zheng, L.; Zhang, M. Investigations on the growing, cracking and spalling of oxides scales of powder metallurgy Rene95 nickel-based superalloy. *Appl. Surf. Sci.* **2011**, *257*, 9762–9767. [CrossRef]

28. Li, Y.W.; Wang, D. High temperature VHCF of a 3rd generation Ni-based single crystal superalloy with different casting pore sizes. *Int. J. Fatigue* **2023**, *175*, 107804. [CrossRef]

29. Brenneman, J.; Wei, J. Oxidation behavior of GTD111 Ni-based superalloy at 900 °C in air. *Corros. Sci.* **2015**, *100*, 267–274. [CrossRef]

30. Birks, N.; Meier, G.H. *Introduction to the High Temperature Oxidation of Metals*, 2nd ed.; Cambridge University Press: Cambridge, UK, 2006. [CrossRef]

31. Jones, D.A. Principles and prevention of corrosion. *Mater. Design.* **1992**, *14*, 207. [CrossRef]

32. Chapovaloff, J.; Rouillard, F. Kinetics and mechanism of reaction between water vapor, carbon monoxide and a chromia-forming nickel base alloy. *Corros. Sci.* **2013**, *69*, 31–42. [CrossRef]

33. Pei, H.Q.; Wen, Z.X. Long-term oxidation behavior and mechanism of DD6 Ni-based single crystal superalloy at 1050 °C and 1100 °C in air. *J. Alloy Compd.* **2017**, *704*, 218–226. [CrossRef]

34. Tan, Z.H.; Wang, X.G. Oxidation behavior of a novel Nickel-based single crystal superalloy at elevated temperature. *Vacuum* **2020**, *175*, 109284. [CrossRef]

35. Zhai, Y.; Chen, Y.; Zhao, Y. Initial oxidation of Ni-based superalloy and its dynamic microscopic mechanisms: The interface junction initiated outwards oxidation. *Acta Mater.* **2021**, *215*, 116991. [CrossRef]

36. Yang, L.; Zhou, Z. Effect of Al and Cr on the oxidation behavior of nanocrystalline coatings at 1050 °C. *Corros. Sci.* **2022**, *200*, 110191. [CrossRef]

37. Duval, A.; Miserque, F. Influence of the Oxygen Partial Pressure on the Oxidation of Inconel 617 Alloy at High Temperature. *Oxid. Met.* **2010**, *74*, 215–238. [CrossRef]

38. Evans, H.E. Cracking and spalling of protective oxide layers. *Mater. Sci. Eng. A* **1989**, *120*, 139–146. [CrossRef]

39. Zhao, X.; Wang, Z. Oxidation Property of a Fourth-Generation Powder Metallurgy FGH4108 Nickel-Based Superalloy. *Metals* **2023**, *13*, 945. [CrossRef]

40. Hancock, P.; Hurst, R.C. *The Mechanical Properties and Breakdown of Surface Oxide Films at Elevated Temperatures*, 1st ed.; Plenum Press: New York, NY, USA, 1974. [CrossRef]

41. Evans, H.E.; Lobb, R.C. Conditions for the initiation of oxide-scale cracking and spallation. *Corros. Sci.* **1984**, *24*, 209–222. [CrossRef]

42. He, X.; Peng, X.; Fang, J. Study on the Microstructure and High-Temperature Oxidation Performance of β-NiAl/γ'-Ni$_3$Al Intermetallic Compounds Fabricated by Laser Metal Deposition. *Metals* **2023**, *13*, 1461. [CrossRef]

43. Pilling, N.B.; Bedworth, R.E. The oxidation of metals at high temperatures. *J. Inst. Met.* **1923**, *29*, 529–582.

44. Hahn, J.; Xiao, X.; Lee, D.B. Oxidation of Ni-Cr-Co-Al-Mo-Ti-Re-Ta-W-Ru Single Crystals at 1000 °C in Air. *Korean J. Met. Mater.* **2020**, *58*, 234–246. [CrossRef]

45. Itoh, Y.; Saitoh, M. Influence of high-temperature protective coatings on the mechanical properties of nickel-based superalloys. *J. Mater. Sci.* **1999**, *34*, 3957–3966. [CrossRef]